NANO LETTERS

Letter

pubs.acs.org/NanoLett

Ultrafast Dynamics of Surface Plasmons in InAs by Time-Resolved Infrared Nanospectroscopy

Martin Wagner,[†] Alexander S. McLeod,[†] Scott J. Maddox,[‡] Zhe Fei,[†] Mengkun Liu,[†] Richard D. Averitt,[§,†] Michael M. Fogler,[†] Seth R. Bank,[‡] Fritz Keilmann,[∥] and D. N. Basov*[,†]

[†]Department of Physics, University of California, San Diego, La Jolla, California 92093, United States

[‡]Microelectronics Research Center, The University of Texas at Austin, Austin, Texas 78758, United States

[§]Department of Physics, Boston University, Boston, Massachusetts 02215, United States

[∥]Ludwig-Maximilians-Universität and Center for Nanoscience, 80539 München, Germany

Supporting Information

ABSTRACT: We report on time-resolved mid-infrared (mid-IR) near-field spectroscopy of the narrow bandgap semiconductor InAs. The dominant effect we observed pertains to the dynamics of photoexcited carriers and associated surface plasmons. A novel combination of pump−probe techniques and near-field nanospectroscopy accesses high momentum plasmons and demonstrates efficient, subpicosecond photomodulation of the surface plasmon dispersion with subsequent tens of picoseconds decay under ambient conditions. The photoinduced change of the probe intensity due to plasmons in InAs is found to exceed that of other mid-IR or near-IR media by 1−2 orders of magnitude. Remarkably, the required control pulse fluence is as low as 60 μJ/cm^2, much smaller than fluences of ∼1−10 mJ/cm^2 previously utilized in ultrafast control of near-IR plasmonics. These low excitation densities are easily attained with a standard 1.56 μm fiber laser. Thus, InAs—a common semiconductor with favorable plasmonic properties such as a low effective mass—has the potential to become an important building block of optically controlled plasmonic devices operating at infrared frequencies.

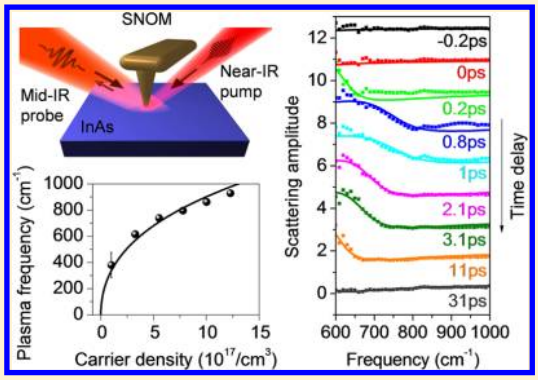

KEYWORDS: *Surface plasmon, semiconductor, pump−probe, ultrafast spectroscopy, near-field microscopy, s-SNOM*

Plasmonics strives to achieve active control of light on length scales below its wavelength.[1−3] Many materials were explored for the purpose of confining and manipulating surface plasmons—collective oscillations of free electrons coupled with light. Early work was heavily focused on noble metals and has uncovered important applications such as plasmonic lasers, nanoantennas, and sensors.[4] However, metals as a plasmonic medium have severe limitations. They are lossy, and their plasmonic characteristics are rigid because the carrier density cannot be altered. Thus, the key plasmonic figures of merit of metals including confinement and propagation length are suboptimal at infrared (IR) frequencies,[5] prompting a broad search for alternative materials.[6,7] One such material, graphene, reveals highly confined mid-IR surface plasmon polaritons that are broadly tunable by adjusting the carrier density.[8−10] Semiconductors share the favorable trait of tunability. An additional benefit of semiconductors is rooted in mature technologies for device implementation. Here, we explored the dynamics of surface plasmons in the prototypical semiconductor InAs by monitoring their time-resolved spectral signatures. We show that this narrow bandgap material reveals excellent plasmonic characteristics in the mid-IR: the frequency range that is important for imaging and chemical recognition of various substances. We demonstrate that the plasmonic behavior governed by the free carrier response can be modulated with unprecedented efficiency on a picosecond (ps) time scale by intense ultrafast light pulses, yet another common aspect with graphene.[11]

We employed scattering scanning near-field optical microscopy (s-SNOM),[12] a technique that excels in probing plasmonic characteristics in real space through nanoimaging[9,10] as well as plasmonic spectra through nanospectroscopy.[8,11] Importantly, s-SNOM allows one to excite plasmons at high momenta[8] without the need for structuring the sample: a mandatory requirement for far-field experiments. Only recently this nanoscale spectroscopy technique based on a commercial s-SNOM (Neaspec GmbH with mid-IR source from Lasnix using Toptica fiber lasers) has been implemented in pump−probe mode, yielding access to plasmonic phenomena at femtosecond (fs) time scales.[11] In the present work we utilize this novel functionality of s-SNOM to monitor the time-resolved spectral signatures of mid-IR surface plasmons in InAs.

Received: April 27, 2014
Revised: July 7, 2014
Published: July 21, 2014

   dx.doi.org/10.1021/nl501558t | *Nano Lett.* 2014, 14, 4529−4534

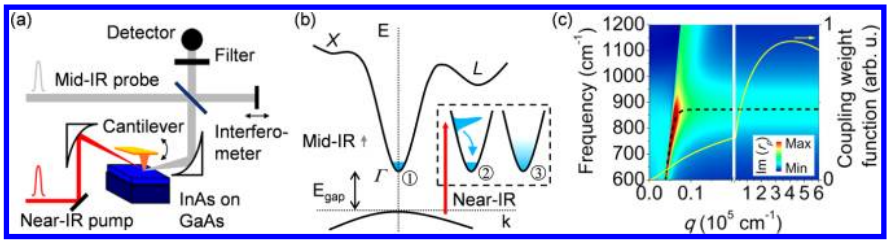

Figure 1. Schematics of the experiment. (a) An InAs film is studied in a scattering scanning near-field optical microscope (s-SNOM). A Michelson interferometer enables mid-infrared (mid-IR) near-field spectroscopy during near-infrared (near-IR) pumping of the sample. (b) InAs band structure scheme representing the energy scales involved in the experiment. The carrier population of the Γ-valley results from doping (1). Near-IR photoexcitation creates a nonequilibrium distribution (inset, 2) which thermalizes into a Fermi−Dirac distribution with elevated carrier temperature (inset, 3) before relaxation back to state (1). (c) Plasmon dispersion evaluated as the imaginary part of the Fresnel reflection coefficient r_p for InAs optical constants described by the Drude model. The black dashed line represents the dispersion for negligible scattering as a guide to the eye. The momentum dependence of the time-averaged near-field coupling weight function[8] for tip radius a = 30 nm is shown as a yellow curve with a maximum close to $q_{tip} \sim 1/a$. Note the different linear scaling of the x-axis close (left) and far (right) from the light line.

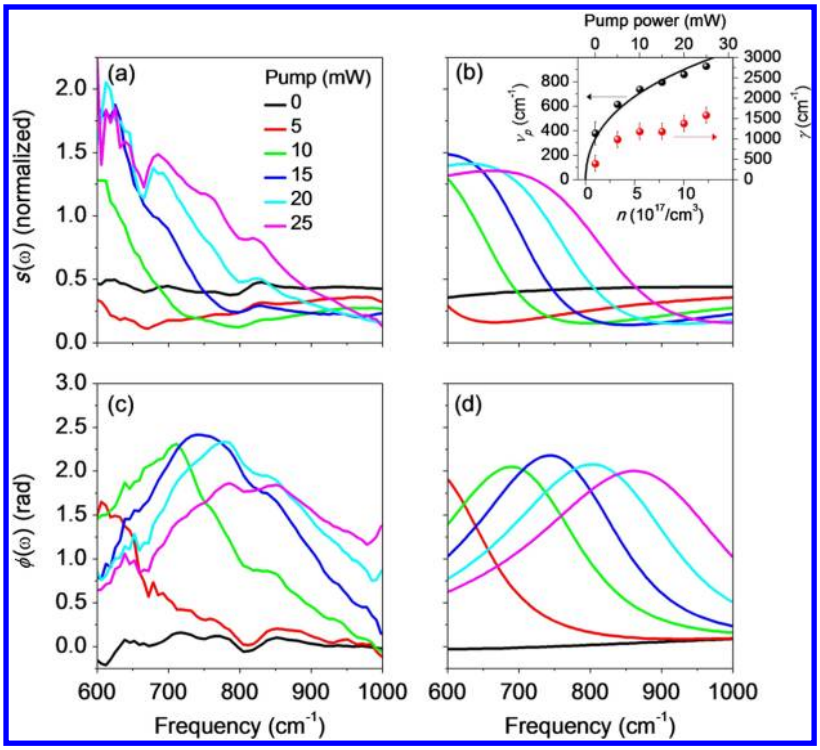

Figure 2. (a, c) Normalized near-field amplitude $s(\omega)$ and phase $\phi(\omega)$ of InAs for different near-IR pump powers. While $s(\omega)$ shows a spectrally flat response without pumping (0 mW pump power in a), the plasmon appears for photoexcitation and shifts to higher frequencies with increasing near-IR pump power. (b, d) Simulated amplitude and phase signal based on the Drude model. The inset in panel b depicts the evolution of the plasma frequency (black dots) and scattering rate (red dots) with carrier concentration. The former agrees well with modeling (black curve) that takes the carrier density dependent effective mass into account.

We show that mid-IR plasmons in InAs can be turned on by a near-IR pump pulse and persist longer than 60 ps: a time interval dominated by recombination at surface defects.[13]

In our experiment (Figure 1a) mid-IR probe pulses in the 600−2200 cm^{-1} spectral range are incident on the metallized s-SNOM tip. The backscattered light contains the near-field contribution which is extracted by demodulating the signal at the second harmonic of the cantilever tapping oscillation at approximately 250 kHz. Spectra of the near-field amplitude $s(\omega)$ and the phase $\phi(\omega)$ are obtained via Fourier transformation of interferograms recorded by an asymmetric Michelson interferometer. Near-IR photoexcitation is provided by synchronized 1.56 μm pulses. The time delay between pump and probe pulses can be varied, and the mid-IR pulse length limits the time resolution to 200 fs. A neutral density filter allows for an adjustable near-IR pump power. We refer to ref 11 for further experimental details. All data were acquired under ambient conditions.

The sample we study is a 2 μm thick InAs film grown by molecular beam epitaxy on a GaAs substrate. The InAs is n-doped to a concentration of $1 \times 10^{17}/cm^3$. As shown below, this equilibrium carrier density is too small to produce a noticeable plasmonic response at mid-IR frequencies. However, optical excitation across the bandgap (Figure 1b) delivers at least an order of magnitude increase of the carrier density. This grants effective dynamical control of the IR plasmon dispersion (Figure 1c) as we will discuss below.

Near-field spectra of InAs acquired at different levels of photoexcitation are shown in Figure 2. The near-field amplitude spectra $s(\omega) = s_{InAs}(\omega)/s_{Au}(\omega)$ in panel a and the

dx.doi.org/10.1021/nl501558t | Nano Lett. 2014, 14, 4529−4534

phase spectra $\phi(\omega) = \phi_{InAs}(\omega) - \phi_{Au}(\omega)$ in panel c are both normalized to the response of a gold film. In the absence of near-IR pumping, both $s(\omega)$ and $\phi(\omega)$ (the black curves in panel a and c, respectively) show a flat, frequency-independent response. The weak feature around 800 cm^{-1} that is apparent in the $s(\omega)$ and $\phi(\omega)$ spectra is also observed in the Au reference data. It is likely to originate from an antenna resonance of the probing AFM tip.[14]

An optical pump in Figure 2a dramatically changes the InAs near-field amplitude. Spectra in Figure 2a were taken at the time delay between near-IR pump and mid-IR probe pulses where the most pronounced changes occurred: approximately 0.8 ps after time overlap. For the 5 mW excitation power we find a mild drop in the $s(\omega)$ signal. Increasing the pump power to 10 mW results in a further drop in the near-field amplitude for frequencies above 750 cm^{-1}, while a pronounced peak appears at the low-energy side of the $s(\omega)$ spectrum. Still higher pump fluences shift this peak toward higher frequencies. At the lowest accessible probe frequencies a 300% increase in scattering amplitude is observed. The phase spectra also exhibit distinct changes. Namely, a broad peak develops on top of the flat phase response and shifts to higher energies with increasing pump fluence.

We attribute the observed spectral features in the InAs near-field response to surface plasmons which couple to the tip of our s-SNOM apparatus.[8] In Figure 1c we illustrate the ability of s-SNOM to probe surface plasmons at high momentum values q without the need of any special coupling techniques.[15] The plasmon dispersion shown in the contour plot is calculated as the imaginary part of the usual, q-dependent Fresnel reflection coefficient r_p.[16] The calculation uses the optical constants of InAs parametrized with the Drude model discussed below including a phenomenological broadening. The Drude model parameters used to evaluate the dispersion in Figure 1c correspond to the case of highest pump power (25 mW). As a guide to the eye the black dashed line marks the dispersion assuming only negligible scattering. In the relevant frequency range the s-SNOM probes finite momenta far beyond the light line as indicated by the momentum distribution of the near-field apparatus (yellow curve) which has a maximum around $q_{tip} \sim 1/a$.[8] We inserted the optical constants that describe the plasmon dispersion into the lightning rod model.[17] This model takes into account the tip−sample interaction (details in the Supporting Information) and allows us to simulate both the near-field amplitude and phase in Figure 2b,d. Reasonable agreement with the experimental data (Figure 2a and c) confirms the assignment of the photoinduced signal to surface plasmons. We note that earlier static s-SNOM studies on chemically doped semiconductors[18−21] have not explicitly attributed the near-field contrast to surface plasmons, although recent near-field modeling and experiments[8−11,16,17,22,23] have established the significance of high-momentum coupling in s-SNOM that we consult for our interpretation.

We now proceed with the quantitative inquiry into the impact of photoexcitation on the near-field spectra. Since the bandgap energy E_{gap} = 0.35 eV of InAs is below the pump photon energy (see schematics in Figure 1b), near-IR photoexcitation creates free electrons and holes at a carrier density Δn in addition to the existing electron doping density n_{static}. The photoinduced signal is dominated by electrons since their effective mass in InAs is as low as $m^* = 0.022m_0$ (with free electron mass m_0) which is much lighter than the heavy-hole mass of $m_{hl} = 0.41m_0$. We will neglect optical transitions from the light-hole band since the density of states compared to the heavy-hole band is small. We express the complex dielectric function ε_{InAs} as a sum of the static and photoinduced contribution and describe these contributions with the common Drude model:

$$\varepsilon_{InAs} = \varepsilon_{static} + \Delta\varepsilon(\Delta n) = \varepsilon_\infty\left(1 - \frac{\omega_p^2}{\omega^2 + i\omega\gamma}\right) \quad (1)$$

where γ is the scattering rate and the plasma frequency ω_p is given by

$$\omega_p = 2\pi\nu_p = \sqrt{(n_{static} + \Delta n)e^2/(m^*\varepsilon_\infty\varepsilon_0)} \quad (2)$$

The constants in eqs 1 and 2 are the elementary charge e, the vacuum permittivity ε_0, and the dielectric constant ε_∞. In our modeling, we treat Δn and γ as adjustable parameters for each pump power. As seen from Figure 2, this approach allows us to reproduce the general trends in our data. The parameters for the plasma frequencies and scattering rates used in modeling are given in the inset of Figure 2b. With increasing pump fluence, both Δn and ν_p increase, as expected. An experimental manifestation of this increase is apparent from the blueshift of the surface plasmon seen in Figure 2a. Additionally, the scattering rate is enhanced at higher pump fluences which is reflected in the broadening of the plasmon feature or, equivalently, in a broader peak in the near-field phase.

Next we analyze the rate at which the plasma frequency is enhanced as a function of the photoexcitation fluence. This analysis takes into account the band nonparabolicity of InAs that leads to a variation of the effective mass with carrier density.[24] Accounting for the established nonlinear increase in m^* with carrier concentration[24] in eq 2 we obtain an accurate fit of the measured pump power-dependent plasma frequency (the black curve in the inset of Figure 2b). Under the constraint that $1 \times 10^{17}/cm^3$ carriers are already present without near-IR pumping, the above fitting procedure allows us to extract the carrier densities for various levels of pump power. This analysis confirms a linear increase of carrier concentration with pump power. Above 10 mW the experimental plasma frequencies are found below the predicted ones, which could indicate the onset of absorption bleaching. The maximum achieved carrier density is $1.2 \times 10^{18}/cm^3$ for 25 mW at an estimated 100 $\mu J/cm^2$ pump fluence. For this carrier concentration the effective mass has increased to $m^* = 0.038m_0$. We remark that we also obtained an accurate fit to our data when using a density-independent, constant effective mass (see the SI). The observed nonlinear behavior of the plasma frequency with pump fluence is entirely dominated by the square root relation of eq 2.

The modeling parameters in the inset of Figure 2b indicate that not only the plasma frequency, but also the scattering rate increases with excitation density. The scattering rate may be written as sum $\gamma = \gamma_0 + \gamma_{eh} + \gamma_{ph}$ where γ_0 is the low carrier density scattering rate associated with impurity scattering from doping, and γ_{eh} and γ_{ph} are the contributions stemming from electron−hole and electron−phonon interactions, respectively.[25] The latter rates γ_{eh} and γ_{ph} are increased with carrier concentration[25,26] and electron temperature.[27] Considering only the electronic heat capacity of a free electron gas, the applied fluence can easily account for an electron temperature of several thousand Kelvin. However, this temperature is certainly reduced at the time of measurement (0.8 ps) due to

dx.doi.org/10.1021/nl501558t | Nano Lett. 2014, 14, 4529−4534

rapid thermalization as discussed below. Note that lattice heating is negligible at the low fluence employed here.[28]

We now turn to the time dependence of the plasmonic near-field response (Figure 3). The symbols in Figure 3a represent

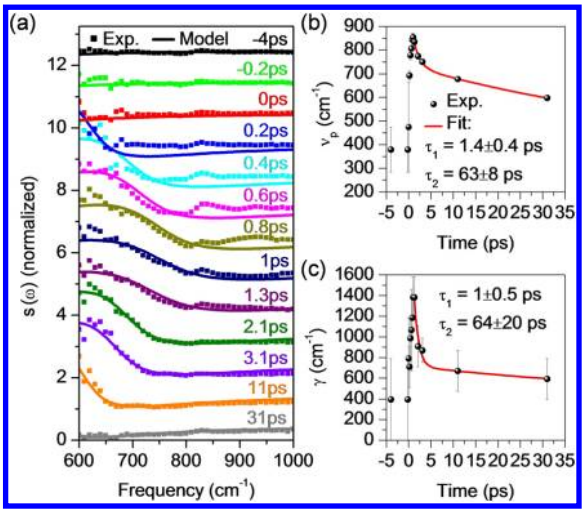

Figure 3. (a) Time-dependent, mid-infrared near-field amplitude normalized to gold for ~18 mW average pump power. From top to bottom the delay between pump and probe pulses is increased. Experimental data are shown as symbols, while theory curves obtained with a Drude model are represented by full lines. Traces are vertically offset for clarity. (b, c) Extracted time-dependent Drude model parameters from panel a. The plasma frequency ν_p (b) and the scattering rate γ (c) are presented together with biexponential fits.

the measured $s(\omega)$ amplitude spectra for 18 mW pump power. From top to bottom, the time delay between the pump and probe pulses is increased, and traces are vertically offset by one unit for clarity. We observe a flat response for a probe pulse preceding the pump pulse by 4 and 0.2 ps (top two traces). At a delay of 0.2 ps after the pump pulse arrival a strong low-frequency shoulder becomes apparent; this feature shifts to higher energies when the probe pulse is delayed further. At a time delay of 1 ps, the plasmonic feature is positioned at the highest frequency and smeared out most prominently, corresponding to a peak value of the scattering rate (Figure 3c). For increasing time delays the broadening decreases while the plasma edge returns to lower energies. After 31 ps (bottom curve) the plasmonic mode has disappeared from the accessible frequency window. The low frequency near-field amplitude is still below the equilibrium value (black, top curve) and has not yet fully recovered on this time scale.

In order to analyze the temporal evolution quantitatively we again employ eq 1. The data displayed in Figure 3a are well-reproduced with solid curves depicting modeling results. The extracted time-dependent plasma frequencies $\nu_p(t)$ and scattering rates $\gamma(t)$ are summarized in Figure 3b and c, respectively. We have also performed biexponential fitting of these traces. We find that both $\nu_p(t)$ and $\gamma(t)$ rise on a subpicosecond time scale, subsequently switching to a fast decay with ~1 ps time constant before slowly decaying with a characteristic time of ~60 ps.

We now discuss the physics of photoexcitation in InAs in light of the new plasmonic data reported here. As apparent from the schematics in Figure 1b, Γ- and L-conduction band minima are separated by 0.73 eV, and near-IR photoexcitation at a pump energy of 0.8 eV is insufficient to directly excite carriers from the valence band into the L-valley. Furthermore, an identical response for probing at full and 10-times reduced mid-IR intensity rules out mid-IR field assisted population of the L-valley[29] where the effective mass is an order of magnitude larger. Thus, the population in the Γ-valley that we probe by its plasmonic response is the dominant effect in our data. Near-IR excitation initially creates a highly nonequilibrium carrier distribution as depicted in Figure 1b where the effective mass is enhanced by a factor of ~2 compared to the conduction band minimum for highest pump fluence.[24,30] The observed ~1 ps long buildup of the plasmon feature reflects the relaxation of these nonequilibrium carriers down to the Γ-valley minimum[31] where their effective mass is smallest and their plasma frequency is maximized. The time scales of the subsequent plasmon dynamics is consistent with the temporal response of free carriers investigated in far-field experiments and is governed by ~1 ps carrier-lattice cooling and ~60 ps surface defect mediated recombination.[13,32,33] The latter assignment is based on the observation of a constant decay time with increasing fluence (not shown). Our data are consistent with the notion that surface plasmons are mainly impacted by decay due to surface defects that is naturally independent of the fluence. On the contrary, bulk Auger recombination is expected to produce an enhanced decay with increasing fluence.[13] Good agreement between modeling and experimental data is obtained in Figure 3a except at time delays shorter than 1 ps. We attribute these deviations to nonequilibrium carrier distributions and ultrafast electron diffusion away from the interface.[34]

Our work advances previous investigations of mid-IR plasmonics to semiconductors and reports for the first time on ultrafast control of surface plasmons in this technologically significant material class. Table 1 offers a summary of plasmonic modulation in different types of plasmonic media along with relevant figures of merit. In our study the low effective mass of InAs allows for high plasma frequencies under only moderate excitation densities delivered by a standard 1.56 μm fiber laser. The modulation efficiency of the probe intensity due to surface plasmons is unprecedented: an increase in near-field intensity by 1100% is achieved with only 60 μJ/cm^2. For comparison, a fluence of 40 μJ/cm^2 induced a 4% plasmon modulation in graphene, another material with exceptional mid-IR plasmon properties.[11] Metal-based structures for near-IR plasmonics require at least an order of magnitude higher fluence for changes in the few percent range[35,36] and up to ~20% when exploiting the light-induced metallic phase of VO_2 nanoparticles.[37] Similar few percent modulations at mJ/cm^2 fluence were observed in semiconductor structures for near-IR

Table 1. Figures of Merit for Mid-IR and Near-IR Plasmon Modulator Schemes Based on Photoexcitation of Different Materials

	InAs (mid-IR)	graphene (mid-IR)	noble metal (near-IR)
probe intensity modulation	1100% (this work)	4%[11]	3%[36]–90%[40]
pump fluence (mJ/cm^2)	0.06 (this work)	0.04[11]	0.5[36]–10[35]
decay time (1/e)	60 ps (this work)	0.6 ps[11]	0.2 ps[36]–100 ps[40]
plasmon confinement ($\lambda_{light}/\lambda_p$)	not realized yet	50–60[9]	15[44]
		100[43]	

dx.doi.org/10.1021/nl501558t | Nano Lett. 2014, 14, 4529–4534

plasmons[38] or for localized plasmon modes at terahertz frequencies.[39] Combined silicon/gold structures do show larger modulation depths of 90% when tuning the metal plasmon, but this still requires intense pumping of 2.2 mJ/cm^2.[40] These values underline the exceptionally high efficiency of mid-IR plasmon modulation in InAs. We also note that the ability of photocarrier generation at 1.3−1.56 μm wavelengths renders the low bandgap material InAs a promising candidate to connect photonics at telecom wavelengths with mid-IR plasmonics.

Comparing the relevant time scales of plasmonic modulation in different materials in Table 1, we find a subpicosecond response time for InAs that is longer than that of graphene[11] and metals.[35,36] However, this time constant in InAs is a consequence of photoexcitation far above the Γ-point with subsequent carrier relaxation to the Γ-minimum, a process that can be accelerated by injecting electrons closer to the conduction band minimum via lower photon energies. A longer plasmon lifetime in InAs of ∼60 ps compared to graphene and most metal-based schemes might prove advantageous in plasmonic circuits requiring longer propagation lengths or interaction times. Defect-engineering, on the other hand, can provide a means to decrease this value if desired.[41] Spatially resolved, near-field imaging of propagating surface plasmon polaritons in graphene[9,10] has revealed high confinement factors as defined as the ratio of the free-space wavelength to the plasmon wavelength λ_p. However, in our experiment the plasmon dispersion is flat, i.e., $\omega(q) \approx$ const., in the probed momentum range on the right side of the light line (Figure 1c). This implies a vanishing group velocity which inhibits the propagation of plasmons. This fact prevents an observation of real-space standing wave patterns. Future near-field experiments on InAs with appropriate, smaller film thicknesses are needed to explore the real space aspects of plasmon confinement and propagation. Here, significant improvement with stronger photoinduced control over the plasmon dynamics can be expected by increasing the localization of the near-IR pump light, for instance through nanostructuring of the probe tip.[42]

We emphasize that s-SNOM is a technique that allows coupling to a broad momentum range in pristine samples that otherwise can be attained with far-field IR methods only for nanostructured samples with feature sizes smaller than 20 nm. This later postprocessing is technologically challenging and furthermore severely impacts the sample properties.

In summary, near-field spectroscopy has revealed that the prototypical semiconductor InAs can serve as an ultrafast optical modulator for surface plasmons in the mid-infrared spectral region with large modulation efficiencies at low near-infrared pump power. The Drude model of the plasmonic response can accurately reproduce the spectrally resolved plasmon behavior, except at small time delays. The demonstrated control of surface plasmons in a narrow gap III−V semiconductor using s-SNOM that inherently enables coupling to plasmons of finite momenta might prove technologically relevant given the high sophistication of semiconductor technology.

■ ASSOCIATED CONTENT

Supporting Information

Supporting experimental data and theory details. This material is available free of charge via the Internet at http://pubs.acs.org.

■ AUTHOR INFORMATION

Corresponding Author

*E-mail: dbasov@physics.ucsd.edu (D.N.B.).

Notes

The authors declare the following competing financial interest(s): F.K. is cofounder of Neaspec and Lasnix, producers of the s-SNOM and infrared source used in this study. All other authors declare no competing financial interests.

■ ACKNOWLEDGMENTS

Research at UCSD is supported by ONR and AFOSR. Development of near-field instrumentation at UCSD is supported by DOE-BES grant DE-FG03-00ER45799 and AFOSR. M.W. acknowledges financial support by the Alexander von Humboldt foundation. S.J.M. and S.R.B. acknowledge support though a Multidisciplinary University Research Initiative from the Air Force Office of Scientific Research (AFOSR MURI Award No. FA9550-12-1-0488).

■ REFERENCES

(1) Maier, S. A.; Atwater, H. A. *J. Appl. Phys.* **2005**, *98*, 011101-1−011101-10.

(2) Schuller, J. A.; Barnard, E. S.; Cai, W.; Jun, Y. C.; White, J. S.; Brongersma, M. L. *Nat. Mater.* **2010**, *9*, 193−204.

(3) Kauranen, M.; Zayats, A. V. *Nat. Photonics* **2012**, *6*, 737−748.

(4) Stockman, M. I. *Opt. Express* **2011**, *19*, 22029−22106.

(5) Law, S.; Adams, D. C.; Taylor, A. M.; Wasserman, D. *Opt. Express* **2012**, *20*, 12155−12165.

(6) Boltasseva, A.; Atwater, H. A. *Science* **2011**, *331*, 290−291.

(7) Tassin, P.; Koschny, T.; Kafesaki, M.; Soukoulis, C. M. *Nat. Photonics* **2012**, *6*, 259−264.

(8) Fei, Z.; Andreev, G. O.; Bao, W.; Zhang, L. M.; McLeod, A. S.; Wang, C.; Stewart, M. K.; Zhao, Z.; Dominguez, G.; Thiemens, M.; Fogler, M. M.; Tauber, M. J.; Castro-Neto, A. H.; Lau, C. N.; Keilmann, F.; Basov, D. N. *Nano Lett.* **2011**, *11*, 4701−4705.

(9) Fei, Z.; Rodin, A. S.; Andreev, G. O.; Bao, W.; McLeod, A. S.; Wagner, M.; Zhang, L. M.; Zhao, Z.; Thiemens, M.; Dominguez, G.; Fogler, M. M.; Castro Neto, A. H.; Lau, C. N.; Keilmann, F.; Basov, D. N. *Nature* **2012**, *487*, 82−85.

(10) Chen, J.; Badioli, M.; González, P. A.; Thongrattanasiri, S.; Huth, F.; Osmond, J.; Spasenović, M.; Centeno, A.; Pesquera, A.; Godignon, P.; Elorza, A. Z.; Camara, N.; García de Abajo, F. J.; Hillenbrand, R.; Koppens, F. H. L. *Nature* **2012**, *487*, 77−81.

(11) Wagner, M.; Fei, Z.; McLeod, A. S.; Rodin, A. S.; Bao, W.; Iwinski, E. G.; Zhao, Z.; Goldflam, M.; Liu, M.; Dominguez, G.; Thiemens, M.; Fogler, M. M.; Castro-Neto, A. H.; Lau, C. N.; Amarie, S.; Keilmann, F.; Basov, D. N. *Nano Lett.* **2014**, *14*, 894−900.

(12) Atkin, J. M.; Berweger, S.; Jones, A. C.; Raschke, M. B. *Adv. Phys.* **2012**, *61*, 745−842.

(13) Vodopyanov, K. L.; Graener, H.; Phillips, C. C.; Tate, T. J. *Phys. Rev. B* **1992**, *46*, 13194−13200.

(14) Huth, F.; Chuvilin, A.; Schnell, M.; Amenabar, I.; Krutokhvostov, R.; Lopatin, S.; Hillenbrand, R. *Nano Lett.* **2013**, *13*, 1065−1072.

(15) Maier, S. A. *Plasmonics: Fundamentals and Applications*; Springer: New York, 2007.

(16) Dai, S.; Fei, Z.; Ma, Q.; Rodin, A. S.; Wagner, M.; McLeod, A. S.; Liu, M. K.; Gannett, W.; Regan, W.; Watanabe, K.; Taniguchi, T.; Thiemens, M.; Dominguez, G.; Castro Neto, A. H.; Zettl, A.; Keilmann, F.; Jarillo-Herrero, P.; Fogler, M. M.; Basov, D. N. *Science* **2014**, *343*, 1125−1129.

(17) McLeod, A. S.; Kelly, P.; Goldflam, M. D.; Gainsforth, Z.; Dominguez, G.; Thiemens, M.; Fogler, M. M.; Basov, D. N. *arXiv*: 1308.1784v3, **2013**.

(18) Knoll, B.; Keilmann, F. *Appl. Phys. Lett.* **2000**, *77*, 3980−3982.

(19) Huber, A. J.; Keilmann, F.; Wittborn, J.; Aizpurua, J.; Hillenbrand, R. *Nano Lett.* **2008**, *8*, 3766−3770.
(20) Stiegler, J. M.; Huber, A. J.; Diedenhofen, S. L.; Gomez Rivas, J.; Algra, R. E.; Bakkers, E. P. A. M.; Hillenbrand, R. *Nano Lett.* **2010**, *10*, 1387−1392.
(21) Jacob, R.; Winnerl, S.; Schneider, H.; Helm, M.; Wenzel, M. T.; von Ribbeck, H.-G.; Eng, L. M.; Kehr, S. C. *Opt. Express* **2010**, *18*, 26206−26213.
(22) Zhang, L. M.; Andreev, G. O.; Fei, Z.; McLeod, A. S.; Dominguez, G.; Thiemens, M.; Castro-Neto, A. H.; Basov, D. N.; Fogler, M. M. *Phys. Rev. B* **2012**, *85*, 075419-1−075419-8.
(23) Fei, Z.; Rodin, A. S.; Gannett, W.; Dai, S.; Regan, W.; Wagner, M.; Liu, M. K.; McLeod, A. S.; Dominguez, G.; Thiemens, M.; Castro Neto, A. H.; Keilmann, F.; Zettl, A.; Hillenbrand, R.; Fogler, M. M.; Basov, D. N. *Nat. Nanotechnol.* **2013**, *8*, 821−825.
(24) Li, Y. B.; Stradling, R. A.; Knight, T.; Birch, J. R.; Thomas, R. H.; Phillips, C. C.; Ferguson, I. T. *Semicond. Sci. Technol.* **1993**, *8*, 101−111.
(25) Hendry, E.; Koeberg, M.; Pijpers, J.; Bonn, M. *Phys. Rev. B* **2007**, *75*, 233202-1−233202-4.
(26) Sernelius, B. E. *Phys. Rev. B* **1989**, *40*, 12438−12440.
(27) Rode, D. L. *Phys. Rev. B* **1970**, *2*, 1012−1024.
(28) Callan, J. P.; Kim, A. M.-T.; Huang, L.; Mazur, F. *Chem. Phys.* **2000**, *251*, 167−179.
(29) Ho, I.-C.; Zhang, X.-C. *Appl. Phys. Lett.* **2011**, *98*, 241908-1−241908-3.
(30) Dixon, J. R.; Ellis, J. M. *Phys. Rev.* **1961**, *123*, 1560−1566.
(31) Beard, M. C.; Turner, G. M.; Schmuttenmaer, C. A. *Phys. Rev. B* **2000**, *62*, 15764−15777.
(32) Elsaesser, T.; Shah, J.; Rota, L.; Lugli, P. *Phys. Rev. Lett.* **1991**, *66*, 1757−1760.
(33) Othonos, A. *J. Appl. Phys.* **1998**, *83*, 1789−1830.
(34) Johnston, M. B.; Whittaker, D. M.; Corchia, A.; Davies, A. G.; Linfield, E. H. *Phys. Rev. B* **2002**, *65*, 165301-1−165301-8.
(35) MacDonald, K. F.; Sámson, Z. L.; Stockman, M. I.; Zheludev, N. I. *Nat. Photonics* **2009**, *3*, 55−58.
(36) Pohl, M.; Belotelov, V. I.; Akimov, I. A.; Kasture, S.; Vengurlekar, A. S.; Gopal, A. V.; Zvezdin, A. K.; Yakovlev, D. R.; Bayer, M. *Phys. Rev. B* **2012**, *85*, 081401-1−081401-6.
(37) Rini, M.; Cavalleri, A.; Schoenlein, R. W.; López, R.; Feldman, L. C.; Haglund, R. F., Jr.; Boatner, L. A.; Haynes, T. E. *Opt. Lett.* **2005**, *30*, 558−560.
(38) Traviss, D.; Bruck, R.; Mills, B.; Abb, M.; Muskens, O. L. *Appl. Phys. Lett.* **2012**, *102*, 121112-1−121112-4.
(39) Berrier, A.; Ulbricht, R.; Bonn, M.; Gómez Rivas, J. *Opt. Express* **2010**, *18*, 23226−23235.
(40) Caspers, J. N.; Rosenberg, N.; van Driel, H. M. *Opt. Express* **2010**, *18*, 19761−19769.
(41) Carmody, C.; Tan, H. H.; Jagadish, C.; Gaarder, A.; Marcinkevičius, S. *Appl. Phys. Lett.* **2003**, *82*, 3913−3915.
(42) Berweger, S.; Atkin, J. M.; Xu, X. G.; Olmon, R. L.; Raschke, M. B. *Nano Lett.* **2011**, *11*, 4309−4313.
(43) Brar, V. W.; Jang, M. S.; Sherrott, M.; Lopez, J. J.; Atwater, H. A. *Nano Lett.* **2013**, *13*, 2541−2547.
(44) Jablan, M.; Buljan, H.; Soljačić, M. *Phys. Rev. B* **2009**, *80*, 245435-1−245435-7.